journal

J. Am. Ceram. Soc., **80** [8] 2074–2085 (1997)

Micromechanics of Failure Waves in Glass: II, Modeling

Horacio D. Espinosa* and Yueping Xu

School of Aeronautics and Astronautics, Purdue University, West Lafayette, Indiana 47907–1282

Natchater S. Brar

University of Dayton Research Institute, Dayton, Ohio 45469

In an attempt to elucidate the failure mechanism responsible for the so-called failure waves in glass, numerical simulations of plate and rod impact experiments, with a multiple-plane model, have been performed. These simulations show that the failure wave phenomenon can be modeled by the nucleation and growth of penny-shaped shear defects from the specimen surface to its interior. Lateral stress increase, reduction of spall strength, and progressive attenuation of axial stress behind the failure front are properly predicted by the multiple-plane model. Numerical simulations of high-strain-rate pressure-shear experiments indicate that the model predicts reasonably well the shear resistance of the material at strain rates as high as 1×10^6/s. The agreement is believed to be the result of the model capability in simulating damage-induced anisotropy. By examining the kinetics of the failure process in plate experiments, we show that the progressive glass spallation in the vicinity of the failure front and the rate of increase in lateral stress are more consistent with a representation of inelasticity based on shear-activated flow surfaces, inhomogeneous flow, and microcracking, rather than pure microcracking. In the former mechanism, microcracks are likely formed at a later time at the intersection of flow surfaces. in the case of rod-on-rod impact, stress and radial velocity histories predicted by the microcracking model are in agreement with the experimental measurements. Stress attenuation, pulse duration, and release structure are properly simulated. It is shown that failure wave speeds in excess to 3600 m/s are required for adequate prediction in rod radial expansion.

I. Introduction

The use of microscopic surface flaws to explain the low measured strength values of glass compared to its theoretical strength is a well established concept. By contrast, the role of these flaws in the overall material degradation under dynamic loading is not well understood. The generation and propagation of a damage front in dynamically loaded glass samples has been reported by Kanel *et al.*[1] and Brar *et al.*[2] It was experimentally shown that behind this damage front, glass loses shear and tensile strength. It was also shown by Kanel *et al.*[1] that measured stress histories were inconsistent with elastoplastic material behavior. They observed that the difference between maximum and minimum principal stresses did not change sign but rather vanished upon unloading.

Another unusual material response related to the dynamic behavior of glass was identified by Espinosa *et al.*[3] in their studies of Al_2O_3. Plate impact recovery experiments and their numerical simulations revealed that when the material is dynamically loaded to stresses in the range of 1–2 GPa, measurable inelastic deformations occur during compression. Espinosa *et al.*[3] have also shown that the onset of compressive damage is due to progressive slippage along interfaces containing a thin glassy phase and not to microcracking. TEM studies revealed that accumulation of grain boundary shearing leads to the formation of ''Y-shaped microcracks'' emanating from grain-boundary triple points. Furthermore, their numerical calculations show that the speed of propagation of a tensile wave traveling on previously compressed material is not reduced by the compressive-induced inelasticity. This finding contradicts previous interpretations of the Hugoniot elastic limit (HEL) by other investigators. The observed inelasticity in compression, at stress levels well below the HEL of the material, constitutes a new physical phenomenon that has important implications in the description of failure kinetics, rate dependence, and elastic precursor decay in ceramics. Consequently, understanding failure mechanisms in glass is a key aspect in the modeling of inelasticity in ceramics containing a glassy phase.

Three theories have been proposed to explain this so-called failure wave in glass. Kanel *et al.*[1] argued that a system of microcracks intersecting in space is formed during shock compression leading to the formation of blocks with flat surfaces. These authors also reported that the block boundaries presented a weak but not vanishing tensile strength. A second explanation of the observed failure wave phenomenon, based on theories of inhomogeneous plastic flow in amorphous materials (Spaepen,[4] Argon,[5] Steif *et al.*[6]) and experimental observations in indentation testing (Hagan,[7] Lawn *et al.*,[8] Kurkjian *et al.*[9]) was postulated by Espinosa and Brar.[10] Their interpretation consists of the initiation of shear-activated microfaults, planes of loclized plastic deformation, at the impact surface which propagates to the interior of the sample. Within this mechanism, microcracks nucleated at the intersection of microfaults can explain the observed reduced but finite tensile strength behind the failure front. A third hypothesis invoking phase transformation to crystalline or denser phases within the bulk of glass samples was advanced by Raiser and Clifton.[11] Their motivation for postulating phase transformation was based on the fact that their experimental results showed that surface roughness appears to play no role in the formation of failure waves. However, it is known that phase transformation must be accompanied by a discontinuity in material density or volume. Such a discontinuity would result in a discontinuity in longitudinal stress or particle velocity on arrival of the so-called failure wave which has not been observed in any of the studies on glass failure at stress levels below the HEL of the material.

Recently, we have conducted rod recovery experiments in which extensive fragmentation is observed in the recovered

J. J. Petrovic—contributing editor

Manuscript No. 192353. Received September 1, 1995; approved August 28, 1996.
This research was supported by the National Science Foundation through Grant Nos. MSS-9309006 and MSS-9311289 and by the Purdue Research Foundation through Grant No. 690-1282-2001.

*Member, American Ceramic Society.

glass samples (see Espinosa *et al.*[12]). It should be noted that these observations are performed after unloading, and consequently the history of the fragmentation process is not known. Microscopy studies performed on fracture surfaces confirm the formation of mostly planar faults intersecting in space. Furthermore, the fracture surfaces presented features (twist hackles, Wallner lines, and mist hackles) commonly encountered in glass fracture under tension. Post-test X-ray experiments also revealed that the material retains its amorphous structure.

In view of these observations and the existence of several hypotheses about the physics of the problem, it was decided to numerically investigate the failure event by means of a moving damage front originated at the impact surface at the start of the compression pulse. The material degradation is simulated with the multiple-plane microcracking model discussed in Espinosa.[13] It should be noted that under pure compression, all compressive principal stresses, the multiple-plane model can equally represent penny-shaped defects resulting from inhomogeneous flow as well as microcracks. We are aware of only one other simulation of failure waves in glass in which the shear stress and material strength are relaxed to zero behind the failure front (see Kanel *et al.*[1]). The adopted relaxation process was empirically rather than mechanistically justified.

In this investigation a micromechanical study of glass failure due to dynamic microfracture is performed. The study would be of considerable interest in the following: (i) clarification of the mechanisms leading to the observed material failure and their dependence on stress levels, failure front speed, and experimental configuration; (ii) assessment of the role of damage-induced anisotropy, damage kinetics, and state of multiaxial dynamic loading in the observed failure; (iii) development of guidelines for a better characterization of failure mechanisms including the selection of measurable quantities and their locations based on their sensitivity to damage and inelasticity.

In this study, we are concerned with explaining very unique features observed in the dynamic failure of glass when dynamically loaded in the range 4 to 7 GPa. The fact that failure waves in glass are observed at shock stress levels below the HEL poses a challenge to our conventional understanding of failure processes leading to dynamic failure. The longitudinal stress or particle velocity in the shocked specimens undergoes little change behind the failure wave front. The observed loss of dynamic shear and tensile strengths of material behind the failure wave must occur through an inelastic process initiating and evolving under high confining mean stress with all compressive principal stresses.

Recently, Grady[14] measured stress waves profiles of soda–lime glass specimens shock loaded to stress levels of up to 20 GPa using a velocity interferometer for any reflecting surface (VISAR). The shock compression profiles at shock stress levels below HEL (4 to 7 GPa) are unusual in the sense that stress profiles are very unstable. The profiles for shock stress levels above 10 GPa are much smoother, showing a ramplike portion followed by a relatively steep second shock wave. The steepness of this second shock wave increases as the level of the peak shock stress increases. Moreover, the arrival time of the second compression wave is a decreasing function of peak shock stress. Grady postulated that the unstable stress levels recorded in the range 4 to 7 GPa are due to the reported failure wave phenomenon. We agree with this interpretation and we restrict our attention to this shock stress range. Furthermore, it is in this stress range that the unusual features previously described occur. It should be noted that when soda–lime glass is shocked at stress levels above 10 GPa, the particle velocity shows a sigmoidal shape consistent with a nonlinear stress-strain behavior resulting from homogeneous deformation.

II. Modeling

In this section the inelastic response of glass is modeled through a microcracking multiple-plane model based on a dilute approximation (Taylor model). Our formulation overlaps with some theories in which multiple-plane representations of inelasticity are derived, e.g., Seaman and Dein,[15] Bazant and Gambarova,[16] Ju and Lee.[17] In the quasi-static case, Ju and Lee[17] employed a self-consistent method together with an analytical solution for weakly interacting cracks in order to derive inelastic compliances. Unfortunately, the averaging methods used to compute effective moduli do not admit a straightforward extension into the dynamic range.

We next summarize the microcracking multiple-plane model derived in Espinosa.[13] The basic assumption in this model is that microcracking and/or slip can occur on a discrete number of orientations (Fig. 1). Slip plane properties (friction, initial size, density, etc.) and their evolution are independently computed on each plane. The macroscopic response of the material is based on an additive decomposition of the strain tensor into an elastic part and an inelastic contribution arising from the presence of microcracks within the solid. In contrast to scalar representations of damage (e.g., Rajendran[18]), Espinosa's formulation is broad enough to allow the examination of damage-induced anisotropy and damage localization in the interpretation of impact experiments.

For a representative volume V of an elastic solid containing penny–shaped microcracks with a density $N^{(k)}$, the average inelastic strains are given by

$$\boldsymbol{\epsilon}_{ij}^{c} = \sum_{k=1}^{9} N^{(k)} S^{(k)} \frac{1}{2} (\bar{b}_i^{(k)} n_j^{(k)} + n_i^{(k)} \bar{b}_j^{(k)}) \tag{1}$$

where the subindex k is used to label the orientations, $S^{(k)}$ denotes the surface of a microcrack on orientation k, $\mathbf{n}^{(k)}$ the corresponding unit normal, and $\bar{\mathbf{b}}^{(k)}$ the average displacement jump vector across $S^{(k)}$.

If the resolved normal traction acting on the microcracks on orientation k is tensile, the average displacement jump vector resulting from an applied stress field $\boldsymbol{\sigma}$ is given by

$$\begin{aligned}\bar{b}_i^{(k)} &= \frac{1}{S^{(k)}} \int_{S^{(k)}} b_i^{(k)}\, \mathrm{d}S \\ &= \frac{16(1-\nu^2)}{3E(2-\nu)}\, a^{(k)} (2\sigma_{ij} n_j^{(k)} - \nu \sigma_{jl} n_j^{(k)} n_l^{(k)} n_i^{(k)})\end{aligned} \tag{2}$$

in which E and ν are Young's modulus and Poisson's ratio of the uncracked solid, and a^k is the radius of the penny-shaped microcracks on orientation k. By contrast, if the normal traction

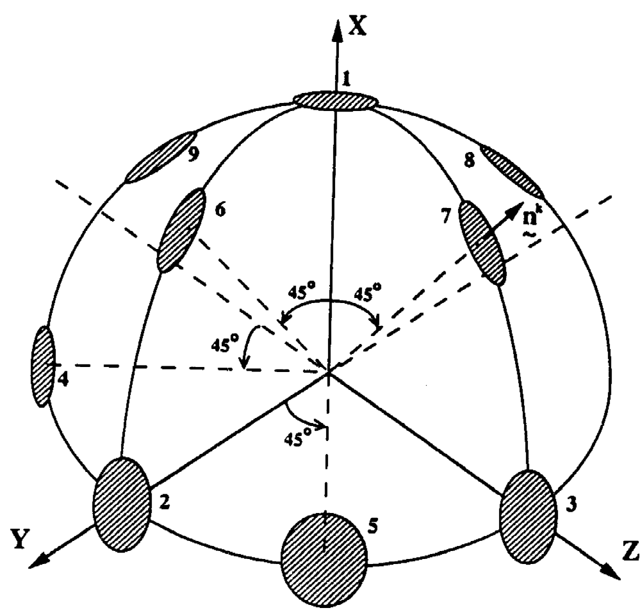

Fig. 1. Schematic of microcracking multiple-plane model.

is compressive, the microcracks are closed and the average displacement jump is given by

$$\bar{b}_i^k = \frac{32(1-\nu^2)}{3\pi E(2-\nu)} a^k f_i^k \tag{3}$$

where $\mathbf{f}^k$ is the effective shear traction vector on orientation k given by

$$f_i^k = (\tau^k + \mu\sigma_n^k)(\mathbf{n}\tau)_i^k \tag{4}$$

in Eq. (4), μ is the friction coefficient of the microcrack faces, τ^k and σ_n^k are the resolved shear stress and the normal stress acting on microcracks with orientation k, respectively, and $\mathbf{n}_\tau^k$ is the unit vector in the direction of the resolved shear traction. Embodied in Eq. (3) is the notion that $\mathbf{f}^k$ provides the effective driving force for the sliding of the microcracks.

In order to compute the inelastic strain tensor at all times, it becomes necessary to follow the evolution of the microcrack radius a^k in the selected orientations. Following Freund,[19] an equation of evolution for a in the case of mixed mode loading can be derived, viz.,

$$\dot{a}^k = m^{\pm} c_R[1 - (K_{IC}/K_{eff}^k)^{n^{\pm}}] \geqslant 0 \tag{5}$$

in which $n^{\pm}$ and $m^{\pm}$ are phenomenological material constants which may have different values in tension and compression, C_R is the Rayleigh wave speed, K_{IC} is the material toughness, and K_{eff}^k is an effective stress intensity factor. For mixed mode conditions, K_{eff}^k is derived by considering an average energy release rate associated with an increase in radius of the microcracks, namely,

$$\mathcal{G}^k = \frac{1}{2\pi}\int_0^{2\pi} \frac{1-\nu^2}{E}\,[K_I^2 + K_{II}^2 + K_{III}^2/(1-\nu)]\,d\theta \tag{6}$$

from which the following expression for K_{eff}^k is obtained:

$$K_{eff}^k = \sqrt{\frac{\mathcal{G}^k E}{1-\nu^2}} \tag{7}$$

The general structure of these constitutive equations corresponds to that of a solid with a damage-induced anisotropic stress–strain relation with elastic degradation. In particular, the effective behavior of the solid is predicted to be rate dependent because of crack kinetics effects. From a computational standpoint, this ensures numerical reliability and mesh independence (Needleman,[20] Espinosa[21]). This is in contrast to quasi-static formulations of damage for which the governing equations become ill-posed in the softening regime (Sandler and Wright[22]). If the material is subjected to a predominantly tensile stress state, microcracks along orientations perpendicular to the direction of maximum tensile stresses will grow according to Eq. (5). In this case, significant dilation is expected due to mode I crack opening. If a predominantly compressive state of stress with shear is imposed, then crack opening is inhibited but inelasticity is manifested by the growth of penny-shaped cracks in modes II and III (shear modes).

III. Numerical Simulation

Before reporting details about the calculations, some background is presented in relation to the glass atomic structure to provide insight into the origin of inelasticity in silicate glasses. Since failure waves have been observed in silicate glasses (soda–lime, borosilicate, and aluminosilicate) of compositions containing silica network modifier ions such as B^+, Na^+, Ca^+, etc., and not in pure silica glass or fused quartz, the atomic structure is likely to play a dominant role in the origin of the observed failure waves. The amount and type of network modifier in different glasses drastically affect their mechanical behavior, especially the plastic flow and fracture characteristics. For example, Young's modulus of soda–lime glass decreases with increasing strain ($dE/d\epsilon < 0$) while that of fused silica increases with increasing strain ($dE/d\epsilon > 0$). Also, fused silica undergoes mainly densification on compression, whereas silicate glasses show slight densification accompanied by considerable inelastic deformation in compression.

Silicate glasses can be considered to consist of hard ordered regions about 2 nm in diameter separated by soft disordered regions. Ainsworth[23] interpreted the hard ordered and softer disordered regions in glass on the basis of the silica network modifiers such as soda (Na_2O) and lime (CaO) present in the basic silica structure. With the addition of network modifiers, the oxygen links at the silica tetrahedron corners are broken. For a combined total of 33% soda and lime, the oxygen link at the corner of each silica tetrahedron is broken. For a further increase in the soda and lime concentration, a second bridge of some of the tetrahedra is broken. With increasing modifier, fewer and fewer tetrahedra are directly linked to other tetrahedra at the three corners. Based on this argument, Ainsworth suggested that the flow strength of soda–lime and other similar glasses is directly related to the proportion of network modifiers in the silica structure. Ernsberger[24] suggested the working hypothesis that plastic flow in glasses occurs by an inhomogeneous mechanism; i.e., large shear displacements occur on certain planes but only elastic straining occurs between these planes. The favor planes on which shear displacement are presumably nucleated have some weak points in the network. According to Argon,[25] the local shear strain in glasses requires relative displacements between neighboring atoms. Since glassy materials are disordered on the atomic scale and contain a distribution of free volume, local shear deformations do not affect the surroundings as strongly as in perfect crystals and are in many instances locally accommodated without long-range effects. This concept permits the development of mechanically isolated local shear deformations in small individual elements of loose atomic packing. Thus, plastic deformation in glassy materials is still a nonlocal form of deformation in comparison with elastic deformation but can be far more local than the corresponding form in crystalline material involving propagating dislocations. These concepts were later extended by Spaepen,[4] Argon,[5] and Steif *et al.*[6] in their work on shear localization in amorphous materials.

Based on the above discussion, the following hypothesis was used in the numerical simulation of failure waves under shock compression. Penny-shaped defects are nucleated within the material due to inhomogeneous shear deformation, regions of local shear deformation in Argon's terminology. Consistently with the experimental observations, the failure wave phenomenon is modeled as a propagating inelastic boundary. This is accomplished by nucleating the penny-shaped defects, with initial size a_0, on elements located behind a failure front that initiates at the sample surfaces and propagates to its interior. The evolution of these defects is modeled based on the equations presented in Section II.

The multiple-plane model has been utilized in the interpretation of the plate and bar experiments conducted on glass specimens. A dynamic finite element analysis is performed to simulate the experiments reported in Espinosa *et al.*,[12] and in Raiser and Clifton.[11] The software used in the calculations is a modified version of the finite element analysis program (FEAP) discussed by Zienkiewicz.[26] A strip of plane strain four-node quadrilateral elements is used in the simulation of normal and pressure-shear experiments. Periodic boundary conditions are imposed to simulate the corresponding deformation fields. In the case of rods, axisymmetric four-node quadrilateral elements are employed. A uniform mesh with an element size of 0.5 mm in the direction of wave propagation is utilized. Symmetry boundary conditions are imposed at the bar axis. In order to preserve axisymmetric conditions, only planes 1, 2, 6, and 8 are included in the analysis (see Fig. 1).

Model parameters like fracture toughness, K_{IC}, are taken from values reported in the literature. Other parameters like defect density are selected such that they are in agreement with

Table I. Summary of Multiple-Plane Model Parameters

Variable	NI	HRPS	UR & CRR	Remarks
K_{IC} (MPa·m$^{1/2}$)	0.5	0.5	0.5	Fracture toughness
a_0 (μm)	1.0	1.0	1.0	Initial crack radius
N_1 (#/m^3)	1×10^{11}	1×10^{13}	1×10^{12}	Crack density on plane 1
N_2 (#/m^3)	1×10^{11}	1×10^{13}	1×10^{12}	Crack density on plane 2
N_3 (#/m^3)	1×10^{11}	1×10^{13}	0×10^{11}	Crack density on plane 3
N_4 (#/m^3)	1×10^{11}	1×10^{13}	0×10^{11}	Crack density on plane 4
N_5 (#/m^3)	1×10^{11}	1×10^{13}	0×10^{11}	Crack density on plane 5
N_6 (#/m^3)	1×10^{11}	1×10^{13}	5×10^{11}	Crack density on plane 6
N_7 (#/m^3)	1×10^{11}	1×10^{13}	0×10^{11}	Crack density on plane 7
N_8 (#/m^3)	1×10^{11}	1×10^{13}	5×10^{11}	Crack density on plane 8
N_9 (#/m^3)	1×10^{11}	1×10^{13}	0×10^{11}	Crack density on plane 9
μ	0.15	0.15	0.15	Internal friction coefficient
m^+	0.3	0.3	0.3	See Eq. (5)
m^-	0.2	0.2	0.2	See Eq. (5)
n^+	0.3	0.3	0.3	See Eq. (5)
n^-	0.1	0.1	0.3	See Eq. (5)

the observations performed on recovered samples (see Espinosa *et al.*[12]). An estimate of the defect density for the case of highly polished surfaces, e.g., rod recovery experiments, can be obtained based on fragment dimensions. In fact, Espinosa *et al.*[12] reported an average fragment size $d = 150$ μm which results in a defect density (assuming only three active orientations) of approximately $1/(3d^3) = 0.99 \times 10^{11}/\text{m}^3$ on each orientation. When such information is not experimentally available, the density is selected consistent with the impact surface roughness. For highly polished surfaces, a density of 1×10^{11} is utilized, while for intentionally roughened surfaces (pressure-shear configuration) a density of $N = 1 \times 10^{13}$ is used. Model parameters used in normal impact (NI), high-strain-rate pressure-shear (HRPS), unconfined rod (UR) and confined rod recovery (CRR) experiments are given in Table I. Young's modulus (E), Poisson's ratio (ν), density (ρ_0), and Rayleigh wave speed (C_R) for soda–lime, aluminosilicate, and borosilicate glasses are given in Table II. Elastic properties, Young's modulus, Poisson's ratio, density, and inelastic properties, initial flow stress (σ_0), reference effective plastic strain (ϵ_0^p), reference strain rate ($\dot{\epsilon}_0^p$), hardening and rate sensitivity exponents (α and β, respectively) for steel, aluminum, and tungsten carbide impactors are given in Table III.

As discussed in Espinosa *et al.*,[12] the sites for crack nucleation are a function of the stress state and geometry of the specimens. For instance, in the case of confined rods, cracks can nucleate not only at the impact surface but also at the rod periphery. This effect has been incorporated into the simulations by selecting different failure wave speeds consistent with experimental records.

Having introduced the model parameters used in the simulations, we next examine the effect of propagating a damage front in the experimental configurations reported in Espinosa *et al.*,[12] and Raiser and Clifton.[11] We start with the lateral gauge configuration, experiment 7-1719. In Fig. 2, the experimentally recorded transverse stresses, through lateral manganin gauges, are compared to the computed stresses for three different values of initial crack size. It can be observed that the stress increase resulting from crack growth, under fully compressive stresses, exhibits different rates as a function of a_0. For $a_0 = 1$ μm the rate of lateral stress increase, at the location of the front gauge, is smaller than the one recorded experimentally. Furthermore, the lateral stress increase upon arrival of the failure wave, at the back gauge, presents a delay with respect to the experimental record. This delay is the result of crack kinetics effects, Eq. (5) in Section II, rather than failure front speed. In all plate impact calculations the failure front has been propagated at a constant speed of 2000 m/s. When the initial crack size is increased to 100 μm, better agreement with the experimentally measured lateral stress increase is obtained. These observations appear to indicate that the propagating failure front consists of the sweeping of propagating defects rather

Table II. Elastic Properties for Three Glasses

Material	E (GPa)	ν	ρ_o (kg/m^3)	C_R (m/s)
Soda–lime glass	72.33	0.24	2700	3167
Aluminosilicate glass	86	0.24	2640	3492
Pyrex glass	64	0.20	2230	3280

Table III. Elastic and Inelastic (J-2 Flow Theory) Properties for Impactor Plates

Material	E (GPa)	ν	ρ_o (kg/m^3)	σ_o (MPa)	ϵ_o^p	$\dot{\epsilon}_o^p$ (s^{-1})	α	β
Steel	207	0.33	8000	800	0.003 865	1000	5	10
Aluminum	69	0.30	2700	300	0.004 384	1000	5	18
WC	550	0.28	14800	5000	0.009 615	1000	3	5

than the nucleation of new ones. In the present simulations, a_0 is the initial defect size nucleated behind the propagating failure front and should not be interpreted as an initial defect in the intact material. The numerically predicted axial stress, σ_x, is also plotted in Fig. 2 for the case $a_0 = 100$ μm. A progressive reduction in axial stress, upon arrival of the failure front, is predicted.

The axial stress behind the failure wave also has distinct features as observed in normal impact experiments with in-material stress measurements close to the impact surface (Espinosa *et al.*[12]). It has been seen that upon arrival of the failure front to an in-material gauge located 3 mm from the impact surface, a progressive reduction in longitudinal stress occurs. This feature can be correlated to the kinetics of the failure process behind its front. In Fig. 3 the computed axial stress trace corresponding to experiment 7-1754, double shock experiment, is compared with the experimental measurement. A small discrepancy in the stress magnitude of the second pulse is seen. However, good agreement is observed in the progressive stress decay produced by the propagating damage front after arrival of the failure wave to the gauge location. The parameters used in this calculation are those previously reported. The failure front was propagated at 2000 m/s.

Normal impact experiments investigating the existence of failure waves have also been reported by Raiser and Clifton.[11] In their experiments the interaction of an unloading wave, from the back surface of a target glass plate, with the advancing failure front was monitored by means of free surface interferometric measurements. Depending on the impactor thickness, spall planes in front and behind the failure front were produced. In Fig. 4, the computed and experimentally recorded free surface velocities for the case in which tensile loading is produced in front of the failure wave are shown. A difference in the rising

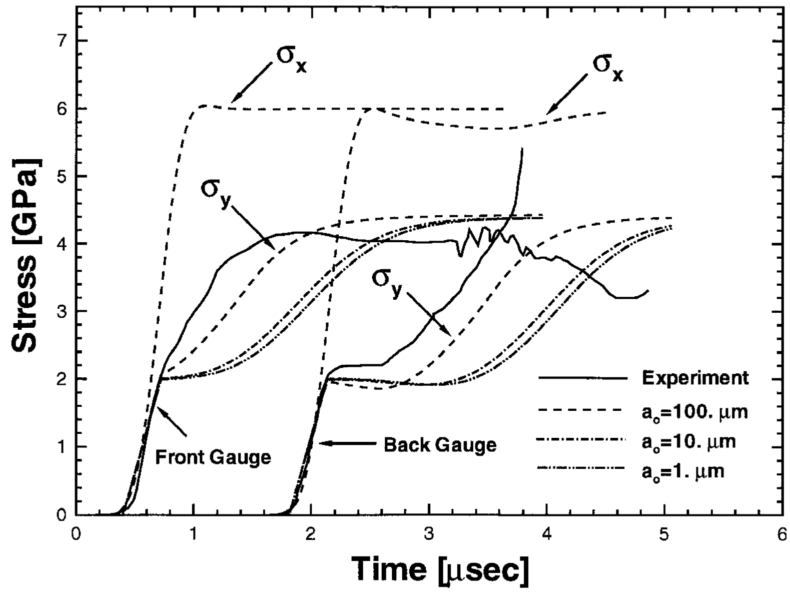

Fig. 2. Transverse stress histories from experiment 7-1719. Comparison between experimental records and simulations with three different initial crack sizes. Lateral and axial stresses are plotted for the case $a_0 = 100$ μm.

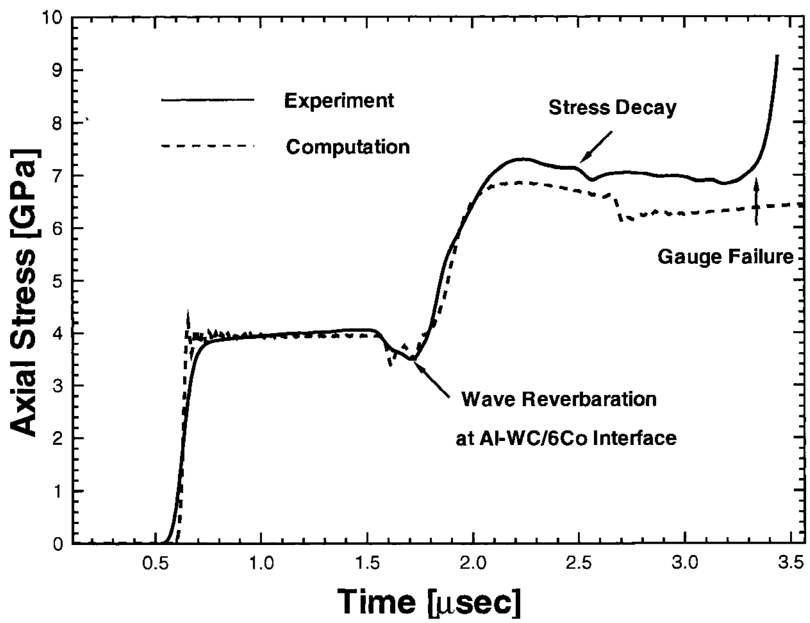

Fig. 3. Longitudinal stress history from experiment 7-1754. Progressive stress decay upon arrival of failure wave to gauge location is observed.

part of the free surface velocity results because glass densification is not incorporated in the present model. Such densification results in a nonlinear material behavior which is manifested by the attenuation of the wave front and the generation of a tail following stress release. Since our main interest is the identification of the failure wave mechanism, we will not account for glass densification in our modeling. From the computed velocities, it is clear that interaction of the unloading wave with the advancing failure front generates waves that result in a reacceleration of the target free surface. In the simulations, two different values of n^+ (see Eq. (5)) have been used to assess the effect of crack growth rate in the free surface velocity. The smaller crack tip velocity, smaller n^+, seems to provide the best fit of the experimental record. The rate of free surface velocity increase is well captured by this simulation. When a higher crack speed is used, the arrival of the second unloading wave, at approximately 1.3 μs, does not become evident in the trace, and the overall reacceleration is excessive.

From these calculations, one can conclude that the free surface reaccleration is produced by crack growth behind the failure front when the material is subjected to tensile dynamic loading. A relevant feature to note is that the increase in free surface particle velocity is progressive; i.e., the material behind the failure front has a reduced but finite spall strength. The case in which the two unloading waves, one from the target back surface and the other from the impactor back surface, meet behind the failure front is examined in Fig. 5. For details of the generated wave fronts in this experiment see Raiser and Clifton.[11] The experimental traces show a fast increase in velocity followed by a plateau with a free surface velocity of 0.9 mm/μs. In the case of experiment Glass 2, a small reacceleration, at approximately 1.1 μs, instead of a velocity reduction, is reported in Raiser and Clifton.[11] This feature indicates the material located at a distance from the failure front exhibits an almost complete loss in spall strength. In experiment Glass 1, a small reduction in free surface velocity is observed at a time

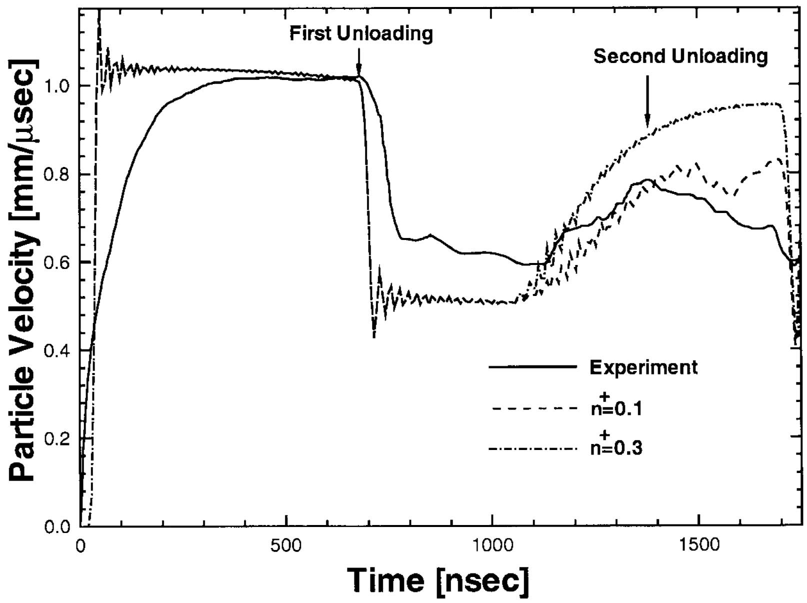

Fig. 4. Free surface particle velocity prediction for experiment 93-04 (see Raiser and Clifton[11]). Increase in particle velocity, after initial unloading, is due to progressive spallation of glass.

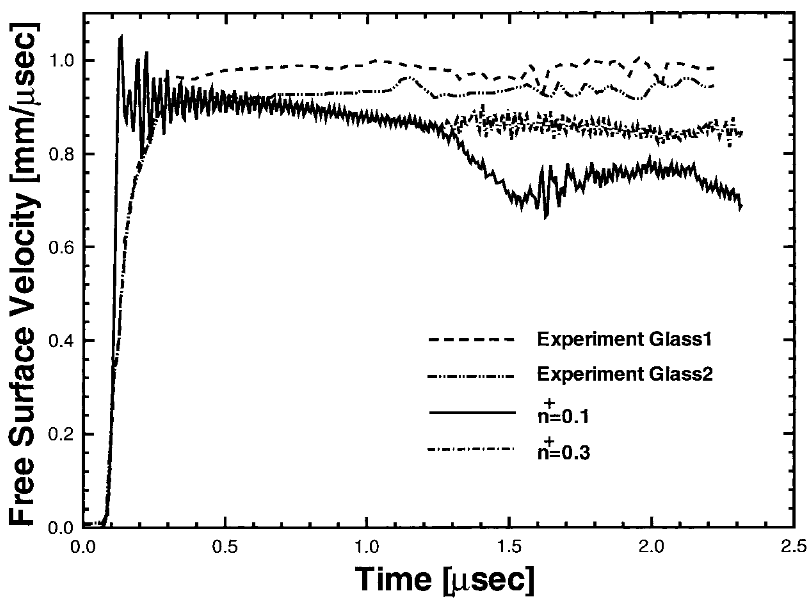

Fig. 5. Free surface particle velocity predictions for experiment Glass 2 (see Raiser and Clifton[11]). The velocity history for experiment Glass 1 is also shown in the same figure. An almost complete loss of spall strength is predicted when $n^+ = 0.3$ is used.

corresponding to the arrival of the unloading wave. When the computed velocity is compared to the experimental record, once again, there is an initial difference in particle velocity due to the fact that our model does not address glass densification. An almost complete lack of spall strength is predicted in our model when $n^+ = 0.3$ is used in the equation for crack evolution. By contrast, when a smaller crack tip velocity is used in the simulations, the material behind the failure front presents a reduced but finite spall strength. It should be noted that the nonlinear behavior induced by glass densification will in general produce a pulse tail that could reduce the decrease in particle velocity observed in the case in which $n^+ = 0.1$. Hence, it appears that modeling of glass densification will provide a more accurate interpretation of these experimental records. Another feature revealed by the numerical simulations is a slow decay in free surface particle velocity after the initial rising part. This decay seems to be linked to the accumulation of inelasticity behind the failure front. Although this feature is not present in the experimental traces reported in Raiser and Clifton,[11] recent experiments performed by Dandekar and Beaulieu[27] appear to confirm our numerical prediction.

Further understanding of the material behavior is obtained by examination of the axial stress–axial strain and pressure–volumetric strain diagrams. A plot of these diagrams for a material point located at the impact surface is given in Fig. 6. For clarity purposes, only the compressive behavior is shown in this figure while the tensile behavior is shown in Fig. 7. The compressive axial stress follows a linear elastic behavior with a small reduction in axial stress accompanied by an important increase in axial strain upon arrival of the failure wave. A small reduction in axial stiffness is observed in unloading as well as a residual inelastic strain. The pressure–volumetric strain curve shows an initial elastic response followed by an increase in pressure originated by the inelastic material response. This

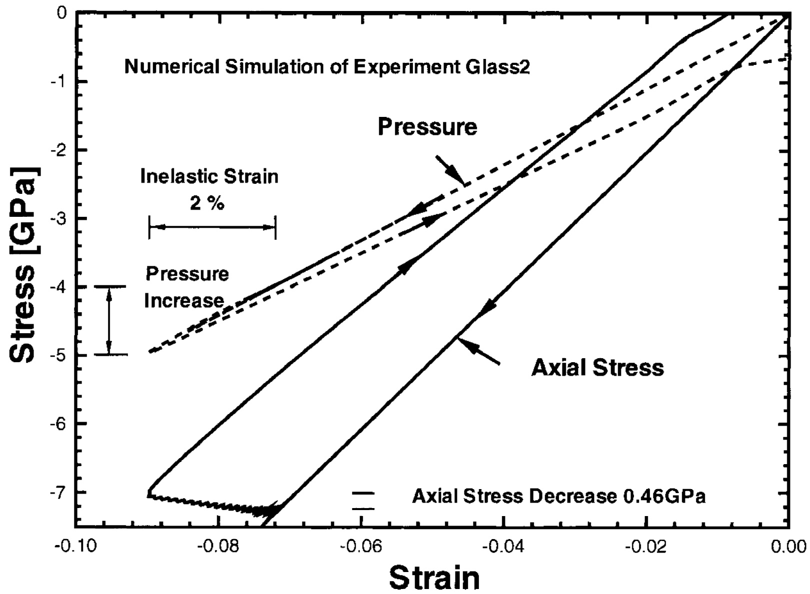

Fig. 6. Axial stress vs axial strain and pressure vs volumetric strain obtained by numerical simulation of experiment Glass 2 (Raiser and Clifton[11]). Only compressive stresses and strains are shown.

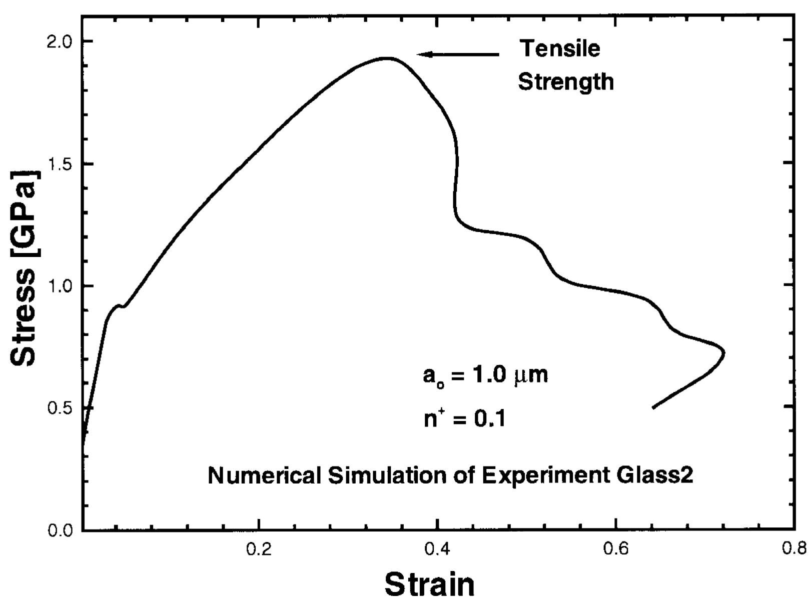

Fig. 7. Axial stress vs axial strain obtained by numerical simulation of experiment Glass 2 (Raiser and Clifton[11]). Only tensile stresses and strains are shown.

pressure increase is consistent with the observed lateral stress increase and substantial shear stress relaxation that accompany the failure wave. A reduction in the slope of the pressure–volumetric strain indicates an increase in material compressibility. It is also observed that full unloading of the axial stress does not result in full unloading of the lateral stress. Figure 6 also reveals that even after an accumulated inelastic strain of 2%, an important stress deviator, difference between axial and mean stresses, exists; i.e., the material preserves some dynamic shear strength. A plot of tensile stress–strain at the same location within the sample is shown in Fig. 7. It can be seen that with the increase in tensile stress the material undergoes major inelastic deformations resulting from growth of microcracks under tensile resolved normal stresses (opening mode). Microcrack opening leads in turn to significant axial strains and moduli degradation. A peak dynamic tensile stress of approximately 1.9 GPa is predicted at this location. A dramatic reduction in stress is observed with the accumulation of damage to a value as low as 0.5 GPa prior to unloading.

Additional insight into glass failure can be gained by modeling the high strain rate pressure–shear experiments reported in Espinosa *et al.*[12] The normal velocity–time profile corresponding to this test is shown in Fig. 8(a). The experimental record exhibits an initial pulse with a short duration, approximately 100 ns, due to the existence of a small gap at the Glass-WC/6Co interface in the flyer assembly. The velocity rise upon closure of the gap is associated with the reverberation of waves within the specimen. Ultimately, a homogeneous state is achieved when the normal particle velocity rises to the value predicted by the elastic impact of the WC/6C anvils. In the numerical simulation of these experiments, the multiple-plane model with the set of parameters previously defined is utilized. Normal motion is applied along the *y*–*y* direction, and shear motion is applied along the *x*–*x* direction (see Fig. 1). We can

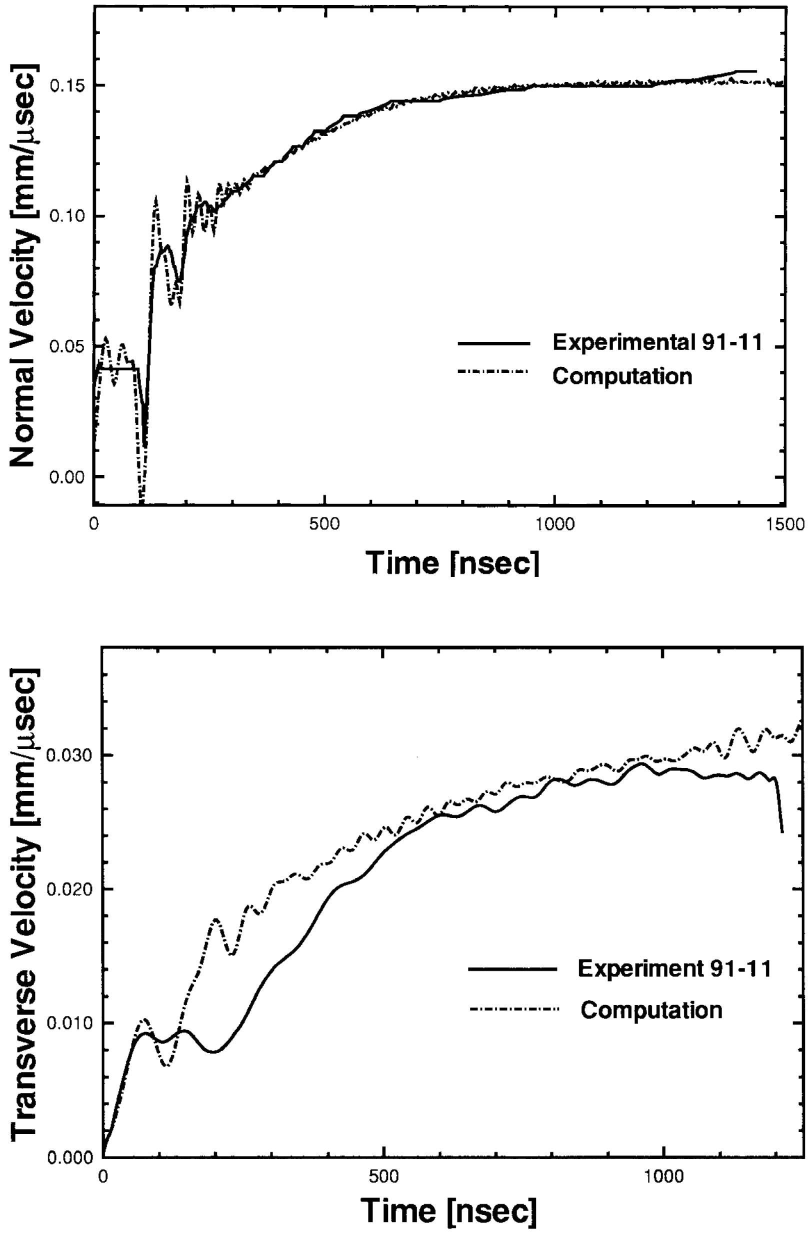

Fig. 8. (a) Normal velocity history from high strain rate pressure-shear experiment, test 91-11 in Espinosa *et al.*[12] Comparison of numerical simulation and experimental record. (b) Transverse velocity history from high-strain-rate pressure-shear experiment, test 91-11 in Espinosa *et al.*[12] Comparison of numerical simulation and experimental record.

observe that the numerical simulation captures the reduction in particle velocity introduced by the specimen–flyer gap as well as the axial stress buildup within the glass sample. The transverse particle velocity, shown in Fig. 8(b), initially rises to a level of 0.01 mm/μs followed by a progressive increase up to a maximum of 0.028 mm/μs. Examination of the computed transverse velocity reveals that the multiple-plane model predicts reasonably well the shear flow of the material as well as the progressive increase in transverse particle velocity with the increase in axial stresses. After gap closure, at approximately 150 ns, the numerical simulations slightly overpredict the rate of transverse velocity increase. This discrepancy can be the result of interface slippage, due to the variations in normal traction introduced by the gap, which is not simulated in the calculations. However, it should be emphasized that good agreement in the dynamic shear resistance of glass, after the initial transient, is obtained. The radius evolutions of the penny-shaped defects, for a material point located at the impact surface on the nine independent orientations, are given in Fig. 9. After the normal stress has reached 90% of its maximum magnitude, at approximately 600 ns, the damage state remains constant in all orientations with the exception of orientations 4 and 5 (see Fig. 9). This observation shows that the shear resistance of glass is controlled by the accumulation of damage on preferred orientations. The additional crack growth observed in orientations 1, 2, 7, and 9, at 1.2 μs, is produced by the arrival of a longitudinal unloading wave originated at the target free surface. The good agreement obtained with the microcracking model is believed to be the result of the model capability in simulating damage-induced anisotropy (Espinosa[13]).

Another experimental configuration used in the identification of failure waves in glass is the rod-on-rod impact configuration (see Espinosa *et al.*[12]). In Fig. 10 the axial stress history obtained in an unconfined soda–lime glass rod experiment, shot 7-1661, is shown. This record has been obtained by embedding a manganin gauge 127 mm from the impact plane. Two numerical simulations are plotted in the same figure, one in which no damage front is propagated, and the other in which two failure fronts, one starting at the impact plane and another

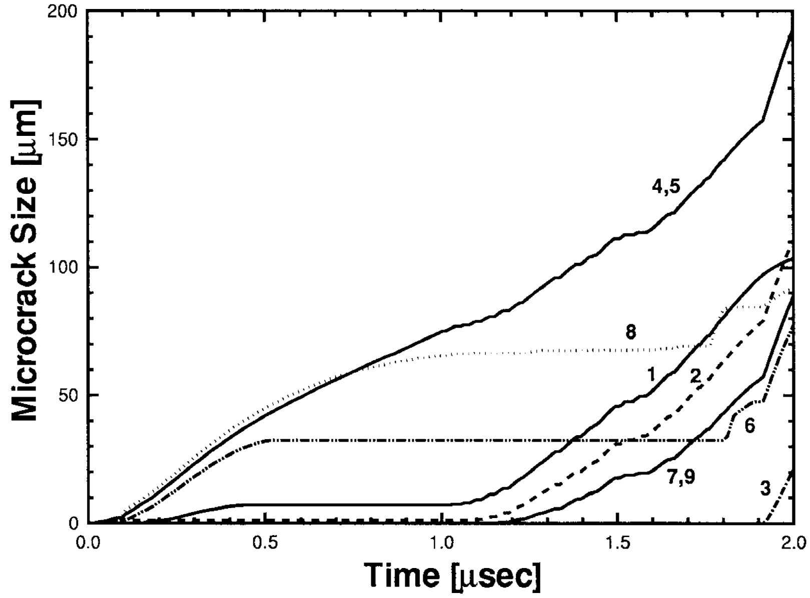

Fig. 9. Crack radius histories of all active orientations predicted by numerical simulation of experiment 91-11.

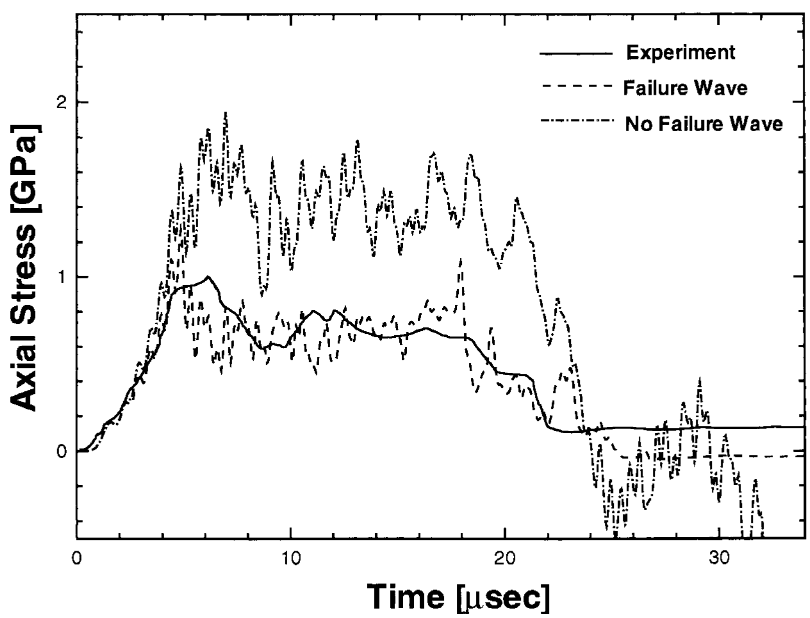

Fig. 10. Comparison of numerical simulations and experimental record for experiment 7-1661.

starting at the gauge plane upon arrival of the stress pulse, are propagated at 3600 m/s. It is observed that in the absence of damage, the compressive axial stress reaches a maximum of approximately 2 GPa, which is almost twice the maximum stress experimentally recorded. By contrast, when the propagation of damage is simulated by means of the microcracking model, the peak stress and pulse structure are well captured. It can also be observed that the stress pulse duration and full unloading are properly predicted.

Simulations performed on a confined soda–lime glass rod on rod recovery experiment, shot 4-1127, are ploted in Fig. 11. In this case the radial velocity of the steel sleeve surface, at 15 mm from the impact plane, is compared with the experimental trace. The numerical prediction reproduces the rising part of the radial velocity up to a peak value of approximately 30 m/s followed by a progressive reduction with well-defined cusps. The numerical result slightly overpredicts the reduction in particle velocity after the initial peak and becomes negative 1.5 μs earlier. Despite these differences, all the features experimentally recorded are very well simulated including the peak positive and negative velocities.

To gain further understanding about the sensitivity of the radial velocity to glass damage, the radial velocity history for three different failure wave speeds and in the absence of microfrature is shown in Fig. 12. It can be seen that in the absence of damage, the reduction in radial velocity after the initial velocity transient differs substantially from the experimental record. These discrepancies become even more obvious at later times. When several wave speeds are examined, it is observed that the best agreement is obtained when a damage front speed of 3600 m/s or higher is used. It should be noted that a failure front speed of approximately 3600 m/s was observed in the fast-framing camera images reported in the companion paper by Espinosa *et al.*[12] for experiment 7-1661. Moreover, this result indicates that in the case of rod experiments, defects nucleate not only at the impact surface but also at the bar

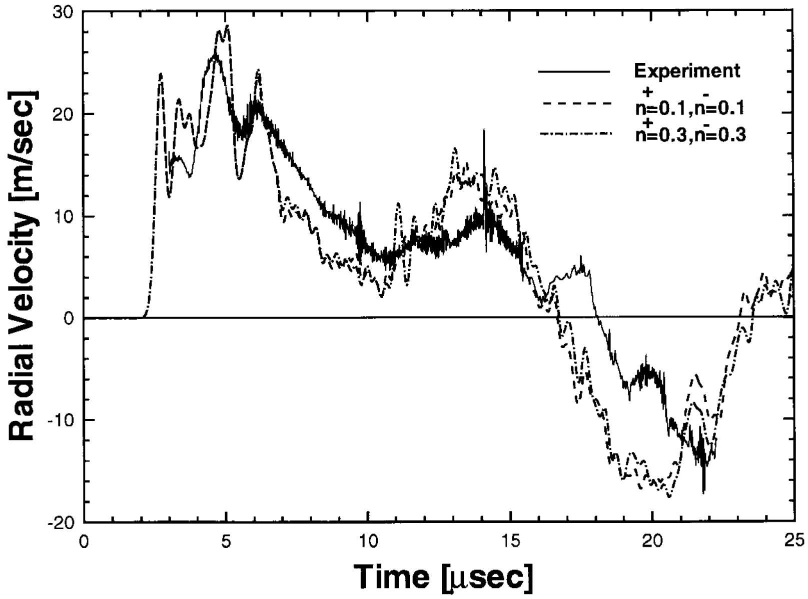

Fig. 11. Plot of radial velocity histories from experiment 4-1127 and numerical simulations. The effect of crack kinetics in the velocity history is examined.

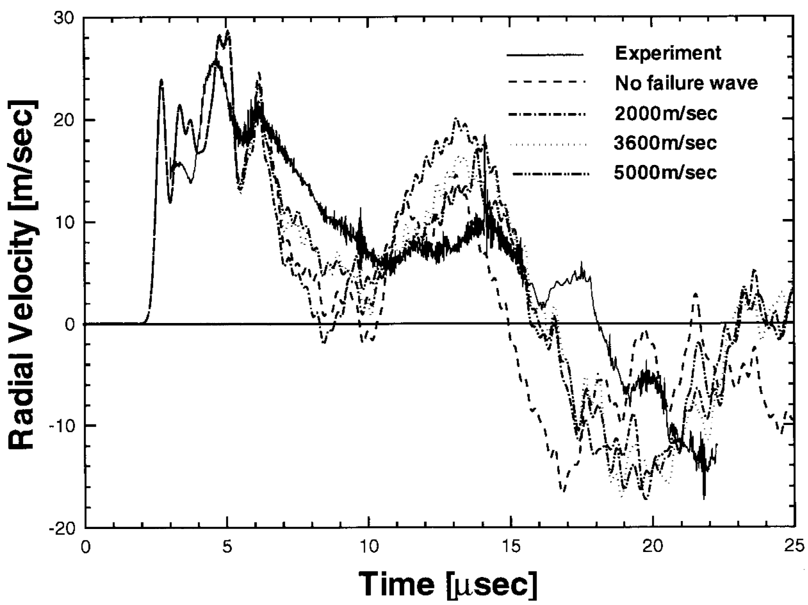

Fig. 12. Plot of radial velocity histories from experiment 4-1127 and numerical simulations. The effect of failure front speed in the velocity histories is examined.

periphery upon passage of the longitudinal pulse. This feature has been discussed in detail in the analysis of experimental records and microscopic observations in Espinosa *et al.*[12]

By examining radial velocity histories, at three different locations along the target rod (see Fig. 13), further understanding of the effect of damage on radial velocities can be gained. We observe important differences in the velocity histories in the first 10 μs. A strong reduction in particle velocity with distance is also observed. This reduction is interpreted as the result of wave attenuation due to damage in the glass rod and plasticity in the steel sleeve.

IV. Concluding Remarks

As stated in the Introduction, one of the main objectives of the present study is the identification and modeling of failure waves in glass. Although we have addressed the failure process by means of a microcracking model, we should note that under fully compressive stress states generated in plate impact experiments, differences between plastic flow in narrow bands and crack propagation under modes II and III are more semantical than physical. Hence, the simulations performed for the case of plate impact experiments are in principle consistent with both microcracking and shear-activated flow (inhomogeneous plastic flow) mechanisms. The main difference between these two hypotheses is that in the former cracks are generated at the start of the compressive pulse, while in the latter cracks are formed at a later time at the intersection of flow surfaces. Physically, in the shear-induced flow mechanism the network of discontinuities behind the failure front exhibits tensile strength.

Our simulations are consistent with previous experimental

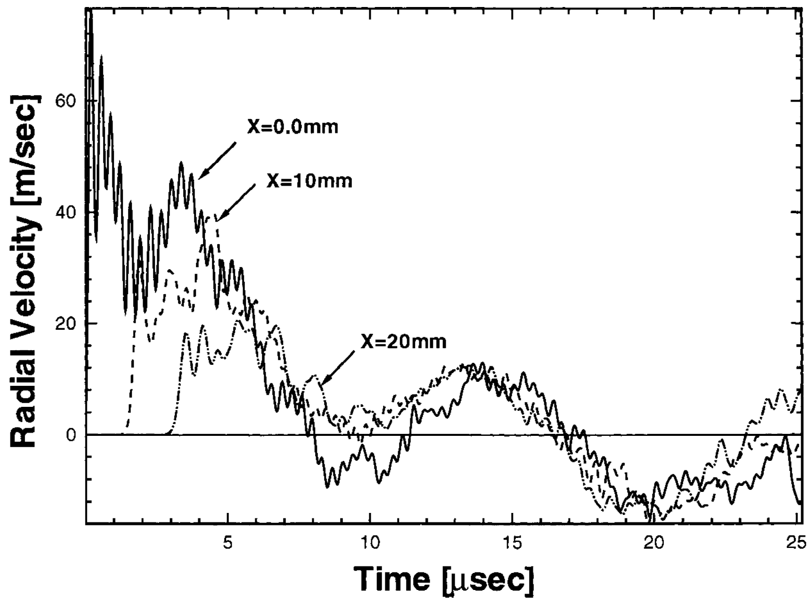

Fig. 13. Plot of radial velocity history variations with distance from impact surface.

observations, although, in our model a reduced but finite spall strength is predicted for small crack tip velocities even at locations well behind the failure front. The progressive spallation of glass at the failure front and its vicinity it is accurately captured by our model. Based on these observations, it seems appropriate to suggest that additional experiments examining the role of compressive pulse magnitude and duration in the residual spall strength behind the failure front are needed. Further experimental work should also examine conditions under which inhomogeneous plastic flow can occur, the role of glass densification in the activation of microcracks or microflow within the material, and the generation of microcracks within the specimen. High-speed photography performed by Senf *et al.*[28] and Bourne *et al.*[29] seems to indicate that defects are nucleated in front of the region in which the material underwent a dramatic reduction in shear strength as recorded by lateral gauges. It is possible that defects are nucleated in the bulk of glass at weak regions in the glass atomic network. However, the results reported by Bourne *et al.*[29] and by Senf *et al.*[28] are inconclusive and require further analysis.

When the experiments reported in the literature and their modeling are analyzed in their totality, the shear-activated flow mechanism appears more likely than the pure microfracture mechanism. We have noted in the discussion of lateral gauge experiments that the failure wave seems to consist of the sweeping of propagating defects, presumably planar, rather than the nucleation and growth of new defects. Moreover, when the previously mentioned progressive spallation behind the failure front is taken into consideration, it appears reasonable to postulate the nucleation, at the intersection of flow planes, of microcracks and their subsequent growth with accumulated inhomogeneous flow in the material. In such mechanisms, the compressive pulse duration and magnitude significantly affects the unloading and tensile loading response of the material. If the failure wave is interpreted as the propagation of a system of cracks from the impact surface to the interior of the specimen, an inconsistency with the observed progressive spallation immediately behind the failure front arises.

Our numerical simulations indicate the measured waveforms reported in the literature appear very useful in the examination of constitutive models and numerical solution schemes. In-material stress measurements, with embedded manganin gauges, are very useful in providing axial stress histories that otherwise cannot be obtained. Stress decay, pulse duration, release structure, and wave dispersion are very well defined by these measurements. High-speed photography is instrumental in the understanding of failure modes. It shows that unconfined glass bars fail by stress-induced microcracking and gives estimates of the failure front speeds. These observations provided the foundation for the modeling presented in this paper. Numerical simulations of confined glass rod recovery experiments indicate that radial velocity histories are also very useful in the identification of damage rate and speed of propagation of the failure wave. Furthermore, these simulations have identified failure front speeds consistent with those recorded in fast-framing camera imaging in the case of unconfined rods.

In summary, this work has examined micromechanical explanations of the so-called failure waves in glass which cannot be investigated by experiments alone. Our study was based on a micromechanical description of inelasticity behind the failure wave rather than its mathematical description in terms of a transformation shock (Clifton[30]). Numerical simulations have shown that a propagating failure front, consisting in penny-shaped planar defects, can capture the main features observed in a variety of impact configurations. Lateral stress increase, reduction of spall strength, and progressive attenuation of axial stress behind the failure wave front are properly reproduced when a multiple-plane microcracking model is utilized. The simulations provide additional insight into the kinetics of the failure process by modeling of wave interaction and damage evolution. Through a parametric study, differences in failure wave speed in plate and rod experiments have been identified, and the reason for such differences discussed in the context of crack nucleation and propagation. The overall agreement between the numerical simulations and the experimental records clearly indicates that the multiple-plane model has the potential to capture the main physics of the dynamic failure process.

References

[1]G. I. Kanel, A. M. Molodets, and A. N. Dremin, ''Investigation of Singularities of Glass Strain Under Intense Compression Waves,'' translated from *Fizika Goreniya i Vzryva,* **13** [6] 906–12 (1977).

[2]N. S. Brar and S. J. Bless, ''Failure Waves in Glass under dynamic compression,'' *High Press. Res.* **10,** 773–84 (1992).

[3]H. D. Espinosa, G. Raiser, R. J. Clifton, and M. Ortiz, ''Experimental Observations and Numerical Modeling of Inelasticity in Dynamically Loaded Ceramics,'' *J. Hard Mater.,* **3** [3–4] 285–313 (1992).

[4]F. Spaepen, ''A Microscopic mechanism for Steady State Inhomogeneous Flow in Metallic Glasses,'' *Act Metall.,* **25,** 407–15 (1977).

[5]A. S. Argon, ''Plastic Deformation in Metallic Glasses,'' *Acta Metall.,* **27,** 47–58 (1979).

[6]P. S. Steif, F. Spaepen, and J. W. Hutchinson, ''Strain Localization in Amorphous Metals,'' *Acta Metall.,* **30,** 447–55 (1982).

[7]J. T. Hagan, ''Shear Deformation under Pyramidal Indentation in Soda–Lime Glass,'' *J. Mater. Sci.,* **15,** 1417 (1980).

[8]B. R. Lawn, T. P. Dabbs, and C. J. Fairbanks, ''Kinetics of Shear-Activated Indentation Crack Initiation in Soda–Lime Glass,'' *J. Mater. Sci.,* **18,** 2785–97 (1983).

[9]C. R. Kurkjian, G. W. Kammlott, and M. M. Chaudhri, ''Indentation Behavior of Soda–Lime Silica Glass, Fused Silica, and Single-Crystal Quartz at Liquid Nitrogen Temperature,'' *J. Am. Ceram. Soc.,* **78** [3] 737–44 (1995).

[10]H. D. Espinosa and N. S. Brar, ''Micromechanical Study of Inelasticity in Brittle and Amorphous Materials,'' proposal submitted to the Army Research Office, Research Triangle Park, NC, 1992.

[11]G. Raiser and R. J. Clifton, ''Failure Waves in Uniaxial Compression of an Aluminosilicate Glass'; pp. 1039–42 in *High Pressure Science and Technology.* Edited by S. C. Schmidt. Joint AIRAPT-APS Conference, Colorado Springs, CO, 1994.

[12]H. D. Espinosa, Y. Xu, and N. S. Brar, ''Micromechanics of Failure Waves in Glass: I, Experiments,'' *J. Am. Ceram. Soc.,* **80** [8] 2061–73 (1997).

[13]H. D. Espinosa, ''On the Dynamic Shear Resistance of Ceramic Composites and Its Dependence on Applied Multiaxial Deformation,'' *Int. J. Solids Struct.,* **32,** [21] 3105–28 (1995).

[14]D. Grady, ''Shock Wave Properties of Brittle Solids''; pp. 9–20 in *APS Proceedings on Shock Compression of Condensed Matter—1995.* Edited by S. C. Schmidt and W. C. Tao. American Institute of Physics, Woodbury, NY, 1995.

[15]L. Seaman and J. L. Dein, ''Representing Shear Band Damage at High Strain Rates''; pp. 229–34 in *Proceedings of the IUTAM Symposium on Nonlinear Deformation Waves (Tallin, Estonia).* Springer-Verlag, Berlin, Germany, 1983.

[16]Z. P. Bazant and P. G. Gambarova, ''Crack Shear in Concrete: Crack Band Microplane Model,'' *J. Struct. Eng. Am. Soc. Civ. Eng.,* **110** [9] 2015–35 (1984).

[17]J. W. Ju and X. Lee, ''On Three-Dimensional Self-Consistent Micromechanical Damage Models for Brittle Solids. Part I: Tensile Loadings,'' *J. Eng. Mech.,* **117** [7] 1495–514 (1991).

[18]A. M. Rajendran, ''High Strain Rate Behavior of Metals, Ceramics, and Concrete,''Air Force Report WL-TR-92-4006, Wright-Patterson Air Force Base, OH, 1992.

[19]L. B. Freund, *Dynamic Fracture Mechanics.* Cambridge University Press, Cambridge, U.K., 1990.

[20]A. Needleman, ''Material Rate Dependence and Mesh Sensitivity in Localization Problems,'' *Comput. Methods Eng.,* **67,** 69 (1988).

[21]H. D. Espinosa, ''Finite Element Analysis of Stress Induced Damage in Ceramics''; M.Sc. Thesis. Brown University, Providence, RI, 1989.

[22]I. S. Sandler and J. P. Wright, ''Strain-Softening''; p. 285 in *Theoretical Foundations for Large Scale Computations of Nonlinear Materials Behavior.* Edited by S. Nemat-Nasser, R. J. Asaro, and G. A. Hegemier. Martinus Nijhoff, Dordrecht, Netherlands, 1984.

[23]L. Ainsworth, ''The Diamond Pyramid Hardness of Glass in Relation to the Strength and Structure of Glass, Part II: Silicate Glasses,'' *J. Soc. Glass Technol.,* **38,** 501T–535T (1954).

[24]F. M. Ernsberger, ''Mechanical Properties of Glass,'' *J. Non-Cryst. Solids,* **25,** 295–321 (1977).

[25]A. Argon, ''Inelastic Deformation and Fracture in Oxide, Metallic, adn Polymeric Glasses''; pp. 79–132 in *Glass Science and Technology, Vol. 5, Elasticity and Strength of Glasses.* Edited by D. R. Uhlmann and N. J. Kriedl. Academic Press, New York, 1984.

[26]O. C. Zienkiewicz, *The Finite Element Method,* 3rd ed. McGraw-Hill, London, U.K., 1977.

[27]D. P. Dandekar and P. A. Beaulieu, ''Failure Wave Under Shock Wave Compression in Soda Lime Glass''; pp. 211–18 in *Metallurgical and Material Applications of Shock-Wave and High-Strain-Rate Phenomena.* Edited by L. E. Murr, K. P. Staudhammer, and M. A. Meyers. Elsevier, Amsterdam, Netherlands, 1995.

[28]H. Senf, E. Straßburger, and H. Rothenhäusler, ''Visualization of Fracture Nucleation during Impact of Glass''; pp. 163–70 in *Metallurgical and Material Applications of Shock-Wave and High-Strain-Rate Phenomena.* Edited by L. E. Murr, K. P. Staudhammer, and M. A. Meyers. Elsevier, Amsterdam, Netherlands, 1995.

[29]N. K. Bourne and Z. Rosenberg, ''The Dynamic Response of Soda–Lime Glass''; pp. 567–72 in *APS Proceedings on Shock Compression of Condensed Matter—1995.* Edited by S. C. Schmidt and W. C. Tao. American Institute of Physics, Woodbury, NY, 1995.

[30]R. J. Clifton, ''Analysis of Failure Waves in Glasses,'' *Appl. Mech. Rev.,* **46** [12] 540–46 (1993). □